Koivumäki, Pasi; Haneda, Katsuyuki; Molisch, Andreas F.

On the Use of Adaptive-Density Point Cloud for Site-Specific Ray-Optics Simulations

Published in:
18th European Conference on Antennas and Propagation, EuCAP 2024

DOI:
10.23919/EuCAP60739.2024.10501282

Published: 01/01/2024

Document Version
Peer-reviewed accepted author manuscript, also known as Final accepted manuscript or Post-print

On the Use of Adaptive-Density Point Cloud for Site-Specific Ray-Optics Simulations

Pasi Koivumäki[1,2], Katsuyuki Haneda[2] and Andreas F. Molisch[1]
[1] University of Southern California (USC), Los Angeles, CA, USA
[2] Aalto University School of Electrical Engineering, Espoo, Finland E-mail: katsuyuki.haneda@aalto.fi

***Abstract*—Multipath channel simulations at millimeter-wave frequencies require more accurate knowledge of the geometry of physical environments than at below-6 GHz frequencies because of the shorter wavelength. The accurate geometry can be obtained as a point cloud through LIDAR (light detection and ranging) scanning of environments. While the use of point clouds for ray-optics simulations of multipath channels has become a popular approach recently, optimized point cloud parameters – for example its density – that allow accurate reproduction of multipath channels are not yet known. Motivated by a conjecture that a same-sized physical object contributes differently to multipath channels when they are near vs far from communicating antennas, we propose to use a point cloud that is denser for environments near antennas and is sparser when further from antennas. Compared to using a uniform-density point cloud with 10 cm resolution on average, the use of such an adaptive-density point cloud in ray tracing simulations shows better reproduction of measured multipath channels, e.g., delay and angular spreads, indicating correctness of our conjecture.**

I. Introduction

Planning of base station deployment and the associated coverage design is an important task of cellular operators. The recent trend of utilizing above-6GHz radio frequencies for broadband mobile cellular requires such design with smaller cell sizes, in typically densely populated areas, than that for below-6GHz frequencies. Semi-deterministic predictions of propagation channels, such as ray tracing, are an important tool for the coverage designs. There has already been works of ray-based radio propagation simulations in urban cellular scenarios for above-6GHz frequencies, e.g., [1]–[18], showing their ability to reproduce the measured cellular coverage and/or radio channel responses. For above-6GHz, a main challenge is the inaccuracies of standard digital maps that describe the physical environments of the cellular site using a limited sets of planar surfaces because they become larger in units of wavelength, depressing the accuracy of the channel prediction.

A promising way of circumventing the low-accuracy maps is to use light detection and ranging (LIDAR). LIDAR scanning provides point cloud representations of a physical environment, from which maps covering a wide area [19] or with a resolution of centimeters or less can be created. It has been shown that the point cloud is usable for site specific multipath radio channel simulations in indoor [1]–[3], [5], [10], [20]–[22] and outdoor [12], [13], [22], [23] scenarios for above-6 GHz frequencies. Thus deterministic simulations using such point clouds are a promising approach, however at the expense of huge increase of computation time due to the fine granularity of the physical environment model. This manuscript therefore proposes a novel approach to decimate points in the point cloud to reduce the computational complexity while reproducing the measured channel responses more accurately than using an ordinal digital map. The validity of the approach is supported by comparison with ground-truth characteristics of the multipath propagation channels obtained from *measurements* at the same site and antenna locations using a directional channel sounder.

The rest of this paper is organized as follows. Section II describes measurements as a reference point for validating channel simulations. Section III introduces point cloud models of physical cellular sites. Section IV presents ray-optics simulations and compares their results with the measurements to study the benefits of using our proposed point cloud density adaptation. Section V concludes the paper, showing that the use of a point cloud model with adaptive density realizes the best reproduction of the measured multipath channels.

II. Radio Channel Measurements

This section describes the measurement campaigns that serve as the ground truth of channel simulations. While the campaigns were partly reported in our earlier papers [13], [24]–[26], the following provides an overview of important specifications of the channel sounder and complementary details of the measurement sites that were not described in earlier papers.

A. Spatio-Temporal Channel Sounder

Our wideband directional channel sounder is based on a vector network analyser (VNA) that allows phase-synchronized measurements of scattering parameters with the radio channels being the device-under-test [27]. The RF signals are centered at 15, 28 and 60 GHz with bandwidth $B = 0.5$, 0.9 and 4 GHz, respectively. The transmit (Tx) antenna is a biconical antenna showing an omni-directional radiation pattern positioned to mainly radiate vertically polarized electric field. Vertically polarized horn antennas with a main lobe gain of 19 dB and half-power beamwidth and hence azimuth angular resolution of 10°, tailored for each frequency band, are installed on the receive (Rx) side. We analyze co-polarized, i.e., Rx-vertical Tx-vertical, propagation channels. The horn antenna is rotated 360° over azimuth in steps of 5°, leading to a directionally-resolved channel impulse response shown in Fig. 1 as an example. The output power from the Tx antenna is 24 dBm. The Tx and Rx antennas are at 2.57 m high from the ground.

B. Measurement Sites

Measurements were performed at the following four sites in the Helsinki metropolitan area, Finland, representing urban microcellular scenarios. All sites had a single Rx location

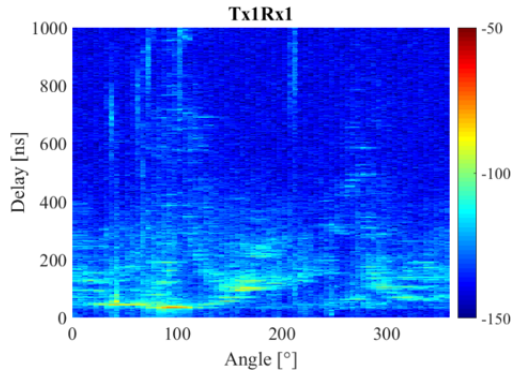

Fig. 1. An example of a measured directional power angular-delay profile.

with the varying number of Tx locations. All measured links had unobstructed optical line-of-sight (LOS) between Tx and Rx. Some vehicular and pedestrian traffic was noted during measurements and acquisition of laser-scanned point clouds.

- *Aleksanterinkatu (AK)* [25] is a street canyon with 8 Tx locations. Two tracks for cars run in the middle of the canyon, which are flanked by pedestrian walkways. Tx-Rx distances ranged from 10 to 188 m. Measurements were performed at 15 and 28 GHz.
- *Itamerenkatu (IM)* is a street canyon with 6 Tx locations, see Fig. 2(b). Four lanes of traffic run in the middle of the canyon, which are flanked by rows of trees and pedestrian walkways. Tx-Rx distances ranged from 10 to 125 m, measurements were performed at 28 GHz.
- *Leppavaarankatu (LV)* is a wide street canyon with 8 Tx locations on both sides of the canyon as shown in Fig. 2(c). Four lanes of traffic run in the middle, flanked by singular trees and pedestrian walkways. Tx-Rx distances ranged from 39 to 131 m. Measurements were performed at 15, 28 and 60 GHz.
- *Narinkkatori (NT)* [13], [24], [28] is an urban square flanked by buildings with 9 Tx locations shown in Fig. 2(d). Tx-Rx distances ranged from 5 to 99 m. Measurements were performed at 15, 28 and 60 GHz.

Aerial photographs of IM and LV are shown in Fig. 2. In each photo, locations of measured Tx and Rx are shown with green and red triangles, respectively.

III. Point Cloud of the Physical Environment

A. Acquisition and Pre-Processing

The point clouds are captured with a 3D laser-scanner[1]. The device uses movable mirrors to steer a laser beam in different directions to detect distances to reflective surfaces. One of the considered physical environments shown in Fig. 3(a) is measured by the laser scanner ending up with a raw point cloud illustrated in Fig. 3(b) with a uniform 1 cm resolution. Figure 3(b) points out typical characteristics of raw point cloud, i.e., 1) shadows cast by objects, e.g., poles in this case, blocking a laser beam, 2) moving objects due to, e.g., a vehicle in this case and 3) missing translucent materials, e.g., glass window. While 2) does not need particular attention, 1) and 3) need to be improved to establish a more complete point cloud, i.e., by 1) combining multiple scans from different locations and 3) supplementing the missing windows through clustering of existing points representing, e.g., window frames. Details of the method is available in [28][2]. The plugin generates a triangular 3D mesh approximating the point cloud, which can be used to generate new points to fill the missing windows. The triangular mesh is used for determining LOS in ray-tracing.

[1]Zoller+Fröhlich GmbH, Z+F IMAGER®5006h.

B. Controlling Point Cloud Density

Point clouds with a varying level of detail can be generated using functionalities of popular software[3]. The point cloud is recursively divided into an octree of cubes until a desired cube side length is reached. Position and normal direction of points contained in each bin of the octree is averaged, effectively applying a smoothing filter and yielding a point cloud with the desired uniform density.

When finding reflected paths *on the point cloud*, e.g., [3], [13], [21], [29], we check if any point falls into the first Fresnel zone formed by a mirror base station and mobile station, according to the image theory. Therefore the use of too-sparse point cloud misses reflected paths, while denser point cloud is not necessary for a far object since a width of the first Fresnel zone w_F increases as

$$w_\mathrm{F} = 2\sqrt{\frac{d_1 d_2}{d}\lambda}, \tag{1}$$

where λ is wavelength and d_1, d_2 and d are defined in Fig. 4. In addition to a uniform-density point cloud of one point in 10 cm on average, we introduce a point cloud with varying density where there are at least 1 point within a cube, i.e., an octree cell, of side length $w_\mathrm{F}/4$ centered at each point. The width w_F is calculated for all points in the point cloud using (1), given the Tx and Rx locations. The coordinates and normal vector directions of points that fall within an octree cell are averaged and represented by a point in the center of the cell. Thereby the point density is higher around the link ends and coarser far away from them. The density also increases for higher frequencies due to decreasing w_F. The density adaptation of the point cloud is required for each Tx-Rx link.

C. Map Based on Public Database

Simple and featureless models of the measured sites are extracted from a public database[4]. In Fig. 3(c), an example of the model is compared with a photograph of the same measured location and a laser-scanned point cloud model. These models consist of planes instead of point clouds.

IV. Comparisons of Simulation and Measurements

This section covers comparison of site-specific wave propagation simulations based on *1) a uniform-density point cloud* with 10 cm resolution on average, *2) adaptive-density point cloud* introduced in Section III-B that achieves 4 points in the first Fresnel zone and lower density outside and *3) a simple featureless map*. The maps were introduced in Section III. The resolution of the raw point cloud was 1 cm.

[2]The Poisson Surface Reconstruction (PoissonRecon) plugin of CloudCompare, https://www.danielgm.net/cc/, was used for 3).

[3]e.g., `pcdownsample()` of the Computer Vision Toolbox in MATLAB and the open-source library TensorFlow.

[4]OpenStreetMap, https://www.openstreetmap.org.

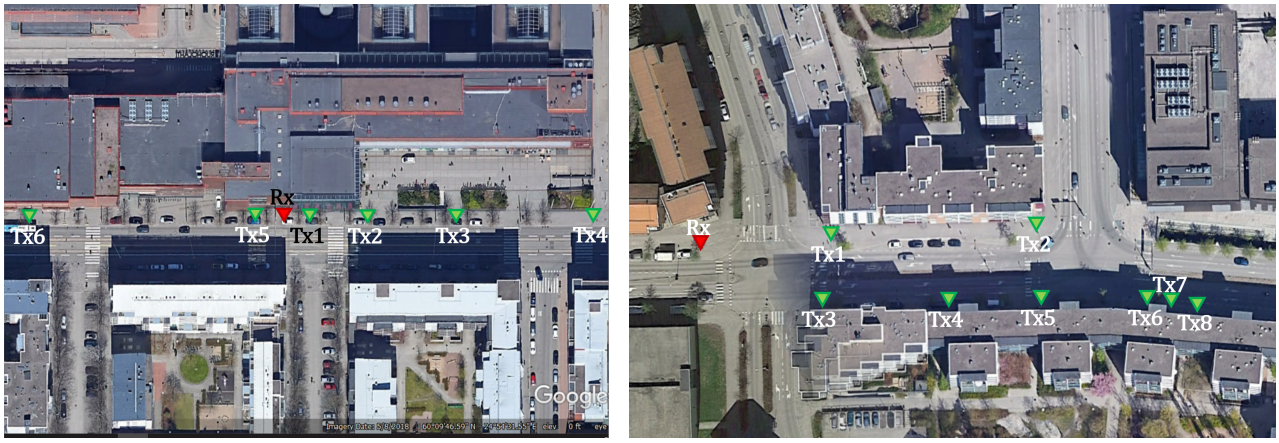

(a) (b)

Fig. 2. Aerial view of two measurement sites with Tx-Rx floor plan for (a) Itamerenkatu (IM) and (b) Leppavaarankatu (LV); © Google Earth for the photos.

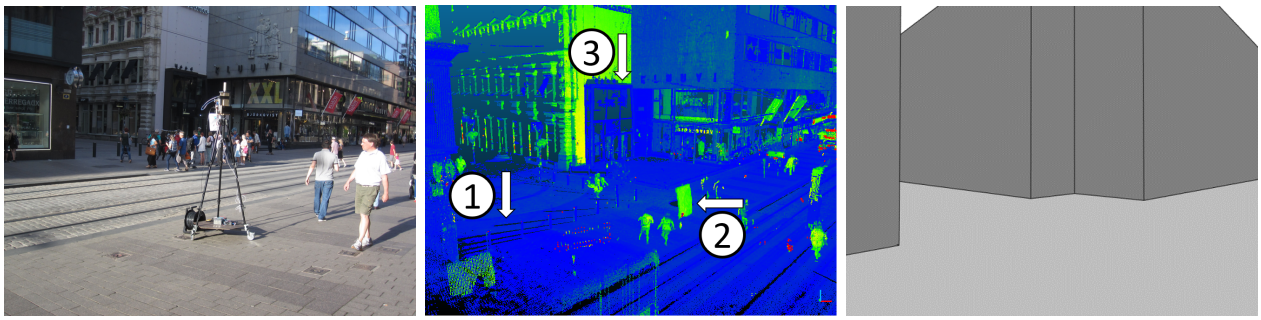

(a) (b) (c)

Fig. 3. A comparison of model types for the channel simulations. (a) Photograph of a measured location Tx4 at AK, with Tx antenna and its tripod in the foreground. (b) Highly detailed laser-scanned point cloud of the same location with pedestrians visible. Features unique to locally acquired laser-scanned point clouds are highlighted with numbered arrows. (c) Simple model extracted from a public database with featureless buildings.

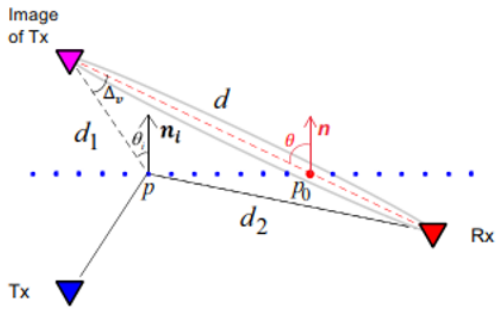

Fig. 4. Definition of the first Fresnel zone.

A. Setup, Assumptions and Comparison Metrics

Ray-tracing simulations using point clouds are based on the image theory [3], [13], [29], [30, Chapter 4], considering up to second order reflections and no diffraction. The point cloud keeps details of facade and moving objects on streets. The latter causes blockage of some propagation paths, where the number of interaction between a path and moving objects are described by a Poisson point process [29] while the blockage loss is calculated by the knife edge diffraction due to absorbing screens having cross section sizes of a human body, tree and a passenger car [31]. A commercially available ray-launcher tool[5], hereafter termed WIS, is used with the simple map from public database. WIS is configured to simulate up to 6 reflections, 1 diffraction and combinations thereof. In all simulations we assume that the physical environment has homogeneous electrical parameters of concrete [32], i.e., the relative permittivity of $\epsilon_r = 5.31$. We do not make distinctions of materials between different sections of the sites or object types, etc. Finally, we assume that the studied sites were in a similar condition during channel sounding and acquisition of the laser-scanned point clouds. For example, density and distribution of pedestrians is assumed comparable.

For meaningful comparison of measured and simulated channels, we consider effects of the channel sounding technique on simulated propagation paths. PADP exemplified in Fig. 1 is reproduced using propagation paths derived from site-specific simulations by convolving them with antenna radiation patterns at link ends in the azimuth domain and with a bandwidth-limited sinc function in the delay domain. For each measured Tx antenna location shown in Fig. 2, we perform 9 ray-optics simulations when the Tx antenna is on a

[5]Wireless InSite, https://www.remcom.com/wireless-insite-em-propagation-software

3×3 grid having 2×2 m^2 area and centered at the measured Tx location. The simulated channel parameters are mean values of those derived in 9 simulations. The following parameters are compared between simulations and measurements: delay spread $\tau_{\rm rms}$, mean delay $\tau_{\rm mean}$, and azimuth spread according to second-central-moment definition S_ϕ [30, Chapter 6].

B. Results and Discussions

Multipath propagation was simulated using our in-house ray-tracing tool with point clouds, and using WIS with planar models of the same site as outlined in Section IV-A. It was on average 10 times faster to simulate multipaths using WIS than using our ray-tracing tool. The simulation runtime compares when using the uniform- and adaptive-density point clouds.

1) Mean Estimates: Table I summarizes the mean values of channel parameters, derived from realizations in different sites and antenna locations. The measured mean values are reproduced best by using the adaptive-density point cloud. However, they are often subject to an outlier of significant errors. Therefore the parameters are also compared against Tx-Rx distance as shown in Fig. 5. Figure 5(a) compares the delay spread $\tau_{\rm rms}$ in AK at 28 GHz. The use of the adaptive-density point cloud performs very well in comparison to the other two models because details of the environment result in rich multipaths. Figure 5(b) shows that the same observation applies to $\tau_{\rm mean}$ in NT at 60 GHz. The angular spread S_ϕ is approximated reasonably by each model in IM at 28 GHz according to Fig. 5(c). WIS provided similar results as the use of adaptive-density point cloud, possibly because the public map contains sufficient influential details of the facade such as varying depth of buildings seen from pedestrian streets.

2) Deviations: Deviation of estimated channel parameters from corresponding measurements is presented in Fig. 6 when using the uniform- and adaptive-density point clouds. The deviation is illustrated in a form of probability density functions along y-axes. Each point in the plot corresponds to the deviation derived from an individual link in one of the cellular sites. Mean and root-mean-square deviation values are shown with white circular and star markers. Vertical gray bars indicate ranges where 50% of values are contained. The figures show that the use of adaptive-density point cloud gives the same extent or smaller deviation than the use of uniform-density point cloud. The deviation of delay-domain parameters $\tau_{\rm rms}$ and $\tau_{\rm mean}$ tends to be smaller as the carrier frequency increases, while the deviation is constant across frequencies for S_ϕ. More outliers were observed when using the uniform-density point cloud than using the adaptive density cloud. The adaptive-density point cloud models objects close to the Tx and Rx antennas precisely, leading to many multipaths originating from there, while distant objects are modeled with less precision, leading to less multipaths. In contrast, the uniform-density point cloud produces a large number of multipaths from distant objects, leading to possible long-delayed phantom paths affecting $\tau_{\rm rms}$ and $\tau_{\rm mean}$. Overall, the use of adaptive-density point clouds appears to produce better results for channel parameters of individual Tx-Rx links.

V. Concluding Remarks

This paper used three digital representations of cellular sites in ray-optics simulations: adaptive-density point clouds, uniform-density point clouds and featureless maps. The first two were derived from point clouds of cellular sites through LIDAR measurements, while the last was from a public map. Using the three types of maps with ray-optics simulators showed that the adaptive-density point cloud yielded the mean delay, delay spread and azimuth angular spread that were closest in many cases to those derived from corresponding measurements. The adaptive density led to denser points near the communicating antennas, while to sparser points in far zones from antennas. It allowed us to consider the important aspect of wave propagation, i.e., a same-sized physical object contributes differently to multipath channels when close to and far from antennas, in the best possible manner among the tested maps and hence led to multipath simulation results best in agreement with measurements.

Acknowledgement

The work was financially supported in part by NIST under grant 60NANB19D121 and NSF under grant 1926913, and Aalto University Foundation for Science and Technology and Electrical Engineering Doctoral School Funding. The authors would like to thank the Nokia Bell-Labs for providing us with the channel sounding data and point cloud of the cellular sites, and Dr. Sinh Nguyen, Dr. Usman Virk, Mr. Jyri Putkonen for help during the measurements and data post-processing.

References

[1] J. Järveläinen and K. Haneda, "Sixty gigahertz indoor radio wave propagation prediction method based on full scattering model," *Radio Science*, vol. 49, no. 4, pp. 293–305, Apr. 2014.

[2] J. Järveläinen, M. Kurkela, and K. Haneda, "Impacts of room structure models on the accuracy of 60 GHz indoor radio propagation prediction," *IEEE Ant. Wireless Prop. Lett.*, vol. 14, pp. 1137–1140, 2015.

[3] J. Järveläinen, A. Karttunen, and K. Haneda, "Indoor propagation channel simulations at 60 GHz using point cloud data," *IEEE Trans. Ant. Prop.*, vol. 64, no. 8, pp. 4457–4467, Aug. 2016.

[4] L. Tian, V. Degli-Esposti, E. M. Vitucci, and X. Yin, "Semi-deterministic radio channel modeling based on graph theory and ray-tracing," *IEEE Trans. Ant. Prop.*, vol. 64, no. 6, pp. 2475–2486, June 2016.

[5] J. Pascual-García et al., "On the importance of diffuse scattering model parameterization in indoor wireless channels at mm-wave frequencies," *IEEE Access*, vol. 4, pp. 688–701, 2016.

[6] M. Inomata et al., "Diffuse scattering prediction for 26 GHz band in indoor office environments," in *Proc. 2017 Int. Symp. Ant. Prop. (ISAP)*, Okinawa, Japan, Oct. 2017, pp. 1–2.

[7] J. W. Wallace et al., "A comparison of indoor MIMO measurements and ray-tracing at 24 and 2.55 GHz," *IEEE Trans. Ant. Prop.*, vol. 65, no. 12, pp. 6656–6668, Dec. 2017.

[8] F. Fuschini et al., "Analysis of in-room mm-wave propagation: Directional channel measurements and ray tracing simulations," *J. Infrared, Millimeter, and Terahertz Waves*, vol. 38, no. 6, pp. 727–744, June 2017.

[9] V. Semkin et al., "Characterization of radio links at 60 GHz using simple geometrical and highly accurate 3-D models," *IEEE Trans. Veh. Tech.*, vol. 66, no. 6, pp. 4647–4656, June 2017.

[10] J. Pascual-García et al., "Wireless channel simulation using geometrical models extracted from point clouds," in *Proc. 2018 IEEE Int. Symp. Ant. Prop. USNC/URSI Nat. Radio Sci. Meeting*, July 2018, pp. 83–84.

[11] F. Mani et al., "26 GHz ray-tracing pathloss prediction in outdoor scenario in presence of vegetation," in *Proc. 12th European Conf. Ant. Prop. (EuCAP2018)*, London, UK, Apr. 2018.

[12] M. Inomata et al., "Radio propagation prediction for high frequency bands using hybrid method of ray-tracing and ER model with point cloud of urban environments," in *Proc. 12th European Conf. Ant. Prop. (EuCAP2018)*, London, UK, Apr. 2018.

[13] P. Koivumäki et al., "A study of polarimetric diffuse scattering at 28 GHz for a shopping center facade," in *Proc. 29th IEEE Int. Symp. Personal, Indoor and Mobile Commun. (PIMRC'18)*, Sep. 2018, pp. 182–187.

[14] E. M. Vitucci et al., "A study on dual-directional Mm-wave indoor channel characteristics," in *Proc. 2019 13th European Conf. Ant. Prop. (EuCAP 2019)*, Mar. 2019, pp. 1–5.

TABLE I
MEAN VALUES OF CONDENSED CHANNEL PARAMETERS ACROSS ALL LINKS AND SITES, FOR EACH FREQUENCY.

	$\overline{\tau_{\text{rms}}}$ [ns]			$\overline{\tau_{\text{mean}}}$ [ns]			$\overline{S_\phi}$ [°]		
f [GHz]	15	28	60	15	28	60	15	28	60
Measured	55.5	50.3	34.0	26.7	25.1	13.6	32.7	28.1	27.5
Adaptive	56.6	44.3	38.1	17.9	15.5	13.8	23.6	23.5	21.4
Uniform	54.2	37.6	34.6	17.2	9.8	7.6	17.8	14.4	13.8
WIS	48.0	42.0	57.1	13.7	14.1	15.3	18.8	20.8	21.8

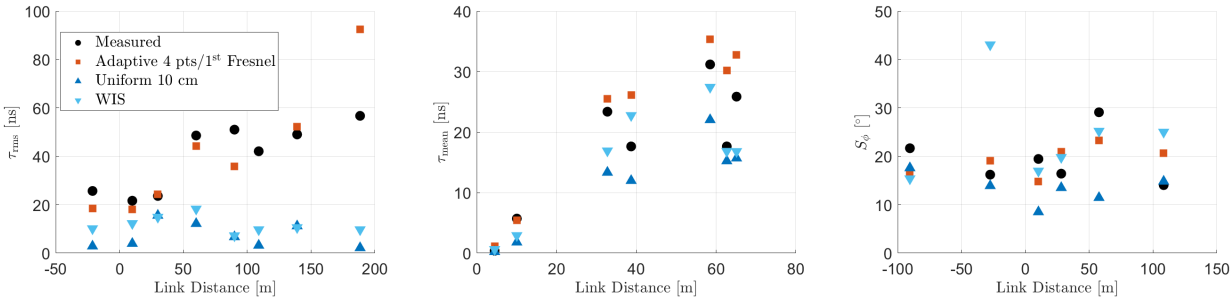

(a) (b) (c)

Fig. 5. Channel parameters shown as a function of link distance: (a) τ_{rms} at 28 GHz measured in AK, (b) τ_{mean} at 60 GHz measured in NT and (c) S_ϕ measured at 28 GHz in IM. Note that negative link distance indicates in an opposite direction along the street canyon to positive distances.

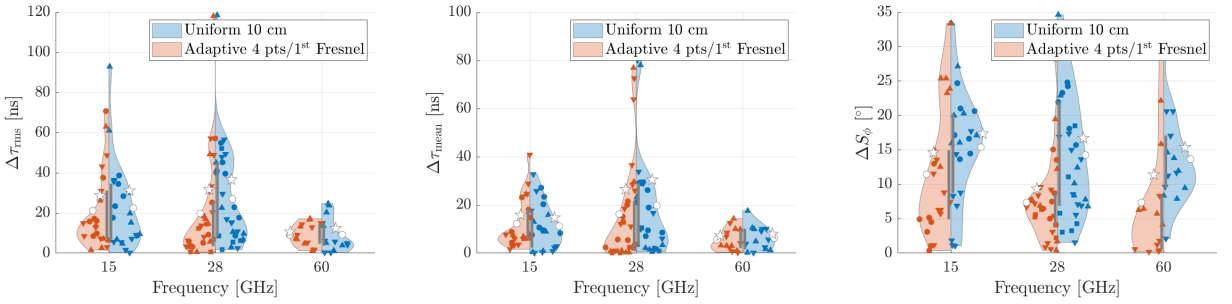

(a) (b) (c)

Fig. 6. Deviation of the simulated channel parameters from corresponding measurements: (a) τ_{rms}, (b) τ_{mean} and (c) S_ϕ. Marker type signifies site where the point originates from: AK (●), IM (■), LV (▲) and NT (▼).

[15] P. Koivumäki and K. Haneda, "Point cloud ray-launching simulations of indoor multipath channels at 60 GHz," in *Proc. 33rd Int. Symp. Per., Indoor and Mobile Radio Commun. (PIMRC 2022)*, 2022, pp. 1–7.

[16] K. Saito et al., "Dynamic propagation simulation method from LiDAR point cloud data for smart office scenario," in *Proc. 33rd Int. Symp. Per., Indoor and Mobile Radio Commun. (PIMRC 2022)*, 2022, pp. 1–6.

[17] W. Okamura et al., "Indoor model reconstruction using 3D point cloud data for ray tracing simulation," in *Proc. 33rd Int. Symp. Per., Indoor and Mobile Radio Commun. (PIMRC 2022)*, 2022, pp. 1–5.

[18] N. Saba et al., "Millimeter-wave radio link analysis for 5G FWA by combining measurements and geospatial data," in *2022 IEEE Future Networks World Forum (FNWF)*, 2022, pp. 433–438.

[19] Y. Egi and C. E. Otero, "Machine-learning and 3D point-cloud based signal power path loss model for the deployment of wireless communication systems," *IEEE Access*, vol. 7, pp. 42 507–42 517, 2019.

[20] U. T. Virk et al., "On-site permittivity estimation at 60 GHz through reflecting surface identification in the point cloud," *IEEE Trans. Ant. Prop.*, vol. 66, no. 7, pp. 3599–3609, July 2018.

[21] U. T. Virk, J. Wagen, and K. Haneda, "Simulating specular reflections for point cloud geometrical database of the environment," in *Proc. 2015 Loughborough Ant. Prof. Conf. (LAPC)*, 2015, pp. 1–5.

[22] M. F. D. Guzman and K. Haneda, "Analysis of wave-interacting objects in indoor and outdoor environments at 142 GHz," *IEEE Trans. Ant. Prop.*, pp. 1–1, 2023.

[23] J. Stephan et al., "Increased reliability of outdoor millimeter-wave link simulations by leveraging Lidar point cloud," in *Proc. 12th European Conf. Ant. Prop. (EuCAP2018)*, London, UK, Apr. 2018.

[24] S. Nguyen et al., "On the mutual orthogonality of millimeter-wave massive MIMO channels," in *Proc. 2015 IEEE 81st Vehicular Technology Conference (VTC Spring)*, 2015, pp. 1–5.

[25] S. L. H. Nguyen et al., "Dual-band multipath cluster analysis of small-cell backhaul channels in an urban street environment," in *2016 IEEE Globecom Workshops (GC Wkshps)*, 2016, pp. 1–6.

[26] M. Peter et al., "Deliverable D2.2 Measurement results and final mmMAGIC channel models," May 2017.

[27] K. Haneda et al., "Estimating the omni-directional pathloss from directional channel sounding," in *Proc. 10th European Conf. Ant. Prop. (EuCAP 2016)*, Davos, Switzerland, Apr. 2016, pp. 1–5.

[28] P. Koivumäki, G. Steinböck, and K. Haneda, "Impacts of point cloud modeling on the accuracy of ray-based multipath propagation simulations," *IEEE Trans. Ant. Prop.*, vol. 69, no. 8, pp. 4737–4747, 2021.

[29] P. Koivumäki et al., "Line-of-sight probability in cluttered urban microcells: Analyses using poisson point process and point cloud," *IEEE Trans. Ant. Prop.*, vol. 70, no. 3, pp. 2161–2173, 2022.

[30] A. F. Molisch, *Wireless Communications - From Fundamentals to Beyond 5 G*, 3rd ed. IEEE Press - Wiley, 2023.

[31] U. T. Virk et al., "Modeling human blockage at 5G millimeter-wave frequencies," *IEEE Trans. Ant. Prop.*, vol. 68, pp. 2256–2266, 2020.

[32] Recommendation ITU-R P.2040, "Effects of building materials and structures on radiowave propagation above about 100 MHz," Aug. 2023.